ELSEVIER

Nuclear Instruments and Methods in Physics Research B 157 (1999) 11–20

NIM B
Beam Interactions with Materials & Atoms

www.elsevier.nl/locate/nimb

Charge transfer and electron emission in ion–surface interactions

U. Thumm [a,*], J. Ducrée [b], P. Kürpick [a,c], U. Wille [d]

[a] *J.R. Macdonald Laboratory, Department of Physics, Kansas State University, Manhattan, KS 66506-2601, USA*
[b] *Institut für Kernphysik, Universität Münster, Wilhelm-Klemm-Str. 9, D-48149 Münster, Germany*
[c] *SAP, D-69190 Walldorf, Germany*
[d] *Bereich Theoretische Physik, Hahn-Meitner-Institut Berlin, Glienicker Str. 100, D-14109 Berlin, Germany*

Abstract

The formation and decay of multiply excited projectiles during collisions of slow *highly charged* ions with metal and insulator surfaces have been simulated based on a classical over-barrier model. Simulations including the full trajectory of the projectile have recently allowed the *simultaneous* evaluation of projectile kinetic energy gains, final charge-state distributions and emitted Auger electron yields in reasonable agreement with experiments. Due to the many-electron nature of these interactions, no detailed quantum mechanical calculations are available. In contrast, for *low charge states* of the incident ion, quantum mechanical close-coupling calculations have been performed that provide detailed information on resonance formation, hybridization, and electron transfer, including the effects of external electric fields. In this paper, some aspects of ion–surface collisions are reviewed within both (many-electron) over-barrier models and quantum mechanical single-electron expansion methods.

PACS: 79.20.Rf; 32.80.R; 34.50.Dy; 34.70.+e
Keywords: Charge exchange; Electron emission; Highly charged ions; Surface scattering; Close-coupling theory

1. Introduction

The detailed theoretical description of interactions between highly charged ions (HCI) and surfaces constitutes a major challenge due to inherent many-body problems and the strongly non-perturbative interactions near the surface. The modeling of the rich physics involved in the formation and decay of multiply excited ('hollow') projectiles is still mostly based on intuition and estimated transition rates, rather than on a detailed quantum dynamical theory. Nevertheless, within the past decade significant progress has been made [1,2], first in understanding the electron capture sequence at large distances from the surface within classical over-barrier models (COMs) [3], and more recently by extending these models in order to obtain a better, though still incomplete, picture of the interaction mechanisms that prevail when an ion moves near or inside a surface [4–7].

Within the same decade, detailed quantum mechanical calculations have become available for interactions of hydrogenic projectiles of low

* Corresponding author. Tel.: +1-785-532-1613; fax: +1-785-532-6806; e-mail: thumm@phys.ksu.edu

0168-583X/99/$ – see front matter
PII: S0168-583X(99)00418-8

charge with surfaces [8–20]. These calculations are limited to a single active electron whose interaction with the many-particle system moving projectile+surface is represented by an effective potential. They provide level shifts, decay rates, and hybridization characteristics. Trends and scaling laws in these results, e.g. the dependence of transition rates on various quantum numbers and on the ion–surface separation D, may be used as input for improved COMs.

In this paper, these complementary theoretical approaches, classical over-barrier models (COMs) (Section 2) and quantum mechanical calculations (Section 3), are outlined. Unless stated otherwise, atomic units are used.

2. Interactions of highly charged ions with surfaces

2.1. Classical over-barrier models

The COM [3] represents the transfer of electrons between valence states of a metal surface and energetically shifted hydrogenic projectile levels in terms of a continuous current of electronic charge. This current sets in at large ion–surface distances D, when the potential barrier of the effective electronic potential $V_{\rm eff}$, which governs the motion of the active electron, drops below the workfunction W of the target. For metal surfaces, $V_{\rm eff}$ includes the potential of the projectile core $V_{\rm proj}$ and classical image potentials $V_{\rm im}$ which model the electronic response of the surface to the external charges of the projectile core ('nuclear image') and active electron ('electron self image').

For insulating targets, the comparatively weaker dielectric response has been accounted for in terms of modified image potentials that involve approximate dielectric functions [6,21]. In addition, the reduced conductivity of insulators may lead to capture-induced positive surface charges. The influence of a trail of localized surface charges on subsequent charge exchange has been included in $V_{\rm eff}$ in terms of the potential $V_{\rm local}$ [6,21,22], such that

$$V_{\rm eff} = V_{\rm proj} + V_{\rm im} + V_{\rm local}. \tag{2.1}$$

The original COM [3] combines estimated rates for resonant over-barrier capture, $\Gamma_n^{\rm RC}$, resonant loss, $\Gamma_n^{\rm RL}$, Auger transitions that fill a particular projectile shell n, $\Gamma_{n',n}^{\rm A\text{-}Gain}$, and Auger transitions that deplete shell n, $\Gamma_{n',n}^{\rm A\text{-}Loss}$, in a system of rate equations for the dynamically changing populations a_n of projectile shells with principal quantum numbers n. Recent extensions include electron transfer and emission processes at small distances D where strong overlap between target and projectile orbitals occurs [5,7,23]. While no detailed quantum dynamical calculations are available, carefully modeled 'side-feeding' (SF) rates $\Gamma_n^{\rm SF}$ can account for the rapid filling of inner projectile shells observed in emitted Auger electron spectra [5,7,24,25] and final charge-state distributions of grazingly reflected projectiles [7,26–28,30].

We have investigated SF based on recently calculated LCV rates for the motion of ion *inside* solids [7,31,32]. LCV processes involve the transition of an electron out of the charge cloud (C), that dynamically follows the projectile as it moves through the substrate electron gas, into a vacancy in the L shell while exciting a plasmon or electron–hole pair in the valence band (V). In order to apply our simulations to very slow collisions, where SF occurs near but outside the surface, we modified these rates to account for varying geometrical overlap. We adopted the interpretation of [31,32], but find best agreement of our simulation results for Al surfaces with experiments (see below), if we use SF rates that exceed the ones given in [31,32] by about an order of magnitude [7].

At distances D comparable with the orbital radius $\langle r_n \rangle$ of resonantly populated high-n shells, strong geometrical overlap may lead to the emission or recapture of projectile electrons. These processes have been modeled in terms of 'peel-off' (PO) rates $\Gamma_n^{\rm PO}$ [29] which become effective *instantaneously*, at the moment when the HCI enters the bulk region. In contrast, we found that mere geometric considerations are not sufficient to model observed final charge-state distributions of reflected projectiles [7]. We included dynamic effects by assuming that a captured electron may be peeled off only after a certain time delay which is related to the electron's orbital period. We also included screening effects by disabling PO for $\langle r_n \rangle$

smaller than the surface screening length, taking into account the diminishing electron density outside the surface.

We modeled the transfer rates for resonant capture and loss according to the original COM [3]. Including PO and SF, the projectile occupation dynamics is now given by a set of rate equations of the form [7]:

$$\frac{da_n}{dt} = \Gamma_n^{RC} - a_n\Gamma_n^{RL} + \sum_{n'>n}\Gamma_{n',n}^{A\text{-}Gain} - \sum_{n'<n}\Gamma_{n,n'}^{A\text{-}Loss} + \Gamma_n^{SF} - a_n\Gamma_n^{PO}. \quad (2.2)$$

The motion of the projectile is determined by the self-image force of the projectile ion and binary Thomas–Fermi–Molière forces between the projectile and individual surface atoms, including recoil effects. For insulator surfaces, the repulsive force of capture-produced surface charges is included.

We calculated binding energies at the Hartree–Fock level. For any projectile configuration vector $\{a_n\}$ occurring along the course of the ion–surface interaction, we employ the Cowan code [33] to generate average configuration binding energies for all (undistorted) projectile shells, $\{\varepsilon_n^\infty(\{a_n\})\}$. Incorporating atomic structure calculations into our simulation requires that the continuous charge current of the original COM is related to transitions of electrons (charge discretization). For the time integration of (2.2) and of Newton's equation for the projectile trajectory $\vec{D}(t)$, we used a Monte-Carlo method with an ensemble of 5000 incident particles [7].

In general, we do not resolve projectile subshell populations. For the L-shell, however, we calculate the 2s and 2p binding energies and keep track of their respective populations. We assume that the 2p level is preferentially populated via Auger ionization (AI) and SF processes, as suggested by its higher degeneracy.

2.2. Image energy gains

The projectile kinetic energy gain due to its self-image interaction is mostly accumulated at large D, where SF and PO do not occur. With regard to metal surfaces, the results of our dynamical COM for 150 keV ions on Au [6] agree well with energy gains measured by Meyer et al. [26] and with the COM simulation of Lemell et al. [34].

Energy gains for 50 keV Xe ions directed under a grazing incidence angle of 1° on alkali halide crystals (LiF and KI) have been measured by Auth et al. [35,36]. Our simulations agree with the experiment for the KI target for $q_p < 17$ (Fig. 1). However, for the LiF target and for low and intermediate incident charge states, the measured values slightly exceed our simulations. Based on the *macroscopic* conductivities of LiF and KI, we assumed that capture-induced surface charges remain localized on the insulator surface during the ion–surface interaction time of about 10^{-14} s or less. In consequence, our numerical results show larger energy gains if we discard surface charges. For KI, the inclusion of capture-induced surface charges appears to improve the agreement with measured energy gains. We note, however, that for significantly shorter decay times of local surface charges – due to possibly much larger local conductivities [37] – the influence of these charges on energy gains may become negligible.

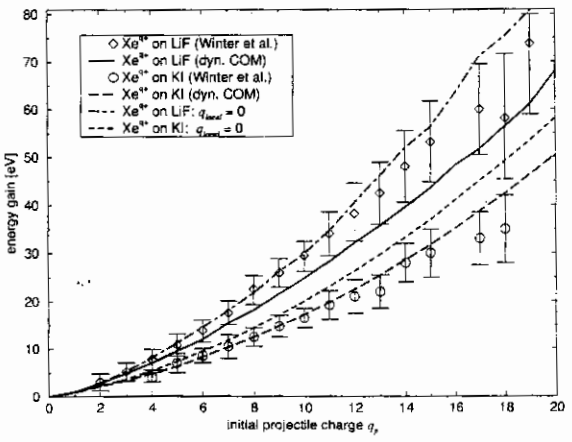

Fig. 1. Experimental energy gains [35,36] compared with our dynamical COM simulations. Results obtained by neglecting capture-induced local surface charges are labeled as $q_{local} = 0$.

2.3. Low-energy electron emission

Fig. 2a shows low-energy electron spectra for N^{6+} interacting with an Al(111) surface under $\Theta = 45°$ for incident energies $E_{kin} = 80$ and 10 eV. The spectra in Fig. 2 are normalized to the total incident particle current. The experimental data have been corrected for the spectrometer transmission and scaled up from emission into the acceptance solid angle of the spectrometer (0.031 sr) to emission into a full 4π sphere. The simulated data have been convoluted with the spectrometer resolution of 0.7%. Integrating the spectral yields above 20 eV leads to yields of $\gamma = 5.7$ and 5.8 emitted electrons per incident ion for the simulated spectra and to $\gamma = 4.9$ and 4.3 for the experiments with $E_{kin} = 10$ and 80 eV, respectively.

Fig. 2b displays AI and SF contributions to the simulated 80 eV spectrum. While the SF mechanism produces a comparatively smooth spectrum for $E < 90$ eV, AI generates structures below 20 eV which we associate with the early stage of projectile relaxation above the surface.

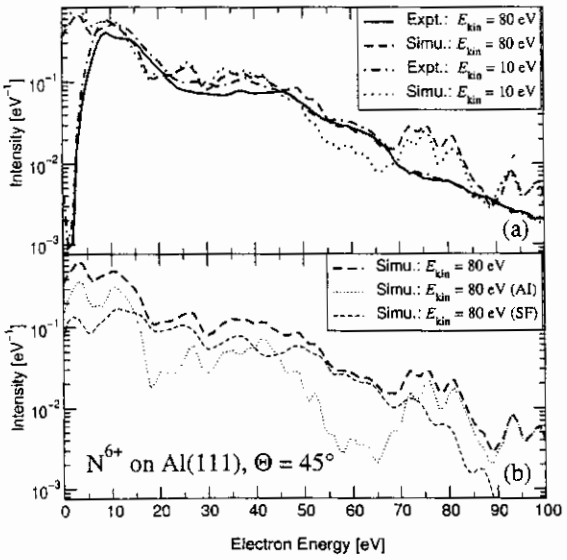

Fig. 2. Low-energy electron spectra for N^{6+} incident under $\Theta = 45°$ on an Al(111) surface for incident energies $E_{kin} = 10$ and 80 eV (a). Subplot (b) also shows SF and AI contributions to the $E_{kin} = 80$ eV spectrum.

2.4. K-Auger spectra

Fig. 3 shows projectile K-Auger spectra for N^{6+} colliding with an Al(111) surface under $\Theta = 45°$ with $E_{kin} = 10$ and 80 eV. The peak widths are related to the range of different initial L-subshell populations at the time of K-Auger decay. In general, the KLL subpeak intensities sensitively depend on the ratio between the L-shell filling rate $\Gamma_L^{fill} = \Gamma_L^{SF} + \Gamma_{n,L}^{AI}$ and KLL decay rates Γ_K^{AI} which are only known for free ions [38,39].

For increasing E_{kin} the KL_1L_1 peak loses intensity which is transferred into the upper part of the KLL spectrum. This can be understood in view of stronger-side feeding into the L shell as the vertex of the trajectory moves closer to the topmost surface layer for increasing E_{kin} [5], resulting in stronger SF at the time of K-Auger emission.

The upper edge of the experimental $KL_{23}L_{23}$ peak is situated at a higher energy than in the simulation. In order to simulate the higher KLL energy, all six neutralizing electrons had to be present in the L-shell. This might indicate that our SF rates, which yield an average L-shell occupation of 4.6 at the time of K-Auger decay for $E_{kin} = 80$ eV, are slightly underestimated.

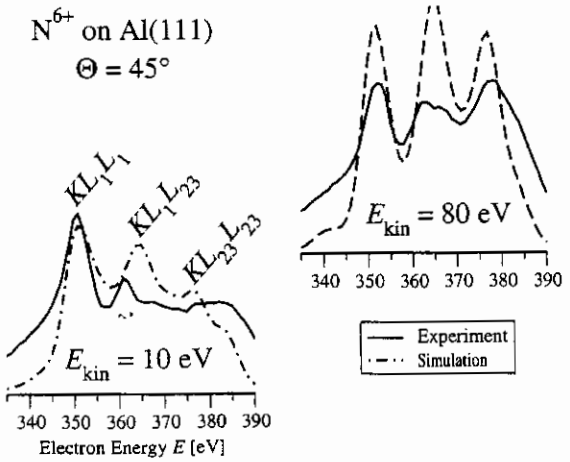

Fig. 3. KLL spectra of N^{6+} incident under $\Theta = 45°$ on an Al(111) surface. Experimental and simulated spectra for incident energies $E_{kin} = 10$ and 80 eV.

2.5. Final charge state distributions

In Fig. 4 we plot the simulated fractions of the final projectile charge states $0 \leqslant q_{\text{final}} \leqslant 2$ for ground state (gs) H-like ions and metastable (mt) He-like second row ions in (1s2s) configurations colliding at $E_{\text{kin}} = 13q$ eV and a grazing angle of $\Theta = 5°$ with Al(1 1 1). Also shown is the measurement by Folkerts et al. [27,28]. Note that the simulation deals with different projectile types containing a single K-shell hole while the experiment refers only to O^{q+}-projectiles with K-shell vacancies for $q \geqslant 7$. We find that the distribution for $q_{\text{final}} = 0$ and 1 mostly varies with the nuclear charge and is rather insensitive to the number of initial K-vacancies.

3. Quantum mechanical approaches to resonance formation and hybridization

We now turn our attention to the detailed quantum mechanical description of a single active electron subject to the interaction with a moving projectile and a metal surface. We employ a time-dependent close-coupling approach based on the expansion of the total wave function in terms of resonance states obtained in the fixed-atom approximation. Jellium wave functions are used to describe the metal states, and the hydrogenic approximation is assumed for the projectile states. In order to simulate the conditions of proposed experiments on resonance ionization of highly excited atoms [40–42], we include a uniform external electric field $\vec{F}$ along the surface normal (equal to the z-axis).

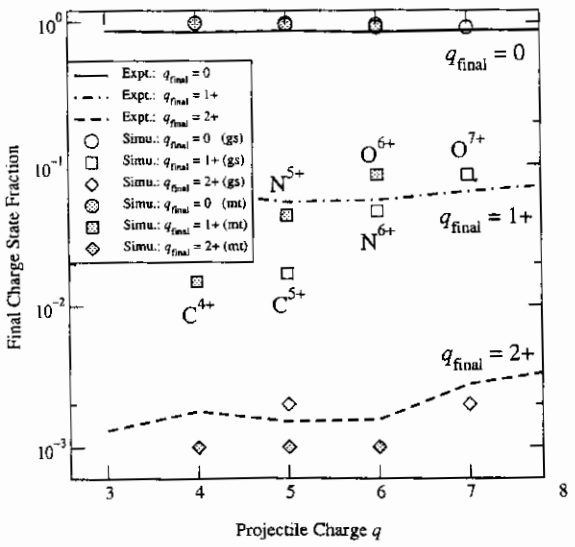

Fig. 4. Final charge state fractions. The lines represent experimental data by Folkerts et al. [27,28] for O^{q+} impinging at $E_{\text{kin}} = 3.75$ keV/amu on Au(110) under surface channeling conditions. The simulation results are for H-like (gs) and He-like (1s2s) metastable (mt) C^{q+}, N^{q+} and O^{q+} ions scattering with $E_{\text{kin}} = 13q$ eV and $\Theta = 5°$ off an Al(1 1 1) surface.

3.1. Two-center close-coupling method

We expand the solution $|\Psi(t)\rangle$ of the time-dependent one-electron Schrödinger equation

$$i|\dot{\Psi}(t)\rangle = \left(T + V_S + V_C^{>}(t) + Fz\right)|\Psi(t)\rangle \tag{3.1}$$

in terms of resonance states $|\phi_j(D(t))\rangle$ [17,43] which depend parametrically on time t via the atom–surface distance $D(t)$,

$$|\Psi(\vec{r};t)\rangle = \sum_{j=1}^{N} c_j(t)|\phi_j(\vec{r};D(t))\rangle \times \exp\left[-\mathrm{i}\int^{t} \mathrm{d}t'\, E_j(D(t'))\right]. \tag{3.2}$$

E_j is the resonance energy, T the kinetic energy, and V_S the surface potential given for $z < z_0$ by the effective bulk potential $-V_0$ and for $z \geqslant z_0$ by $V_{\text{im}}(z;D)$ which includes the electronic self-image potential and the image potential induced by the projectile core. $z_0(D)$ is determined from the condition $V_{\text{im}}(z_0;D) = -V_0$. The Coulomb potential of the atomic core, $V_C^{>}$, is assumed to be fully screened inside the metal.

The basis states $|\phi_j(D)\rangle$ are obtained by solving (3.1) in *fixed-atom* approximation using the self-energy method [17,43]. The self-energy is an optical potential that describes the electronic dynamics in the ionic state space. It includes the coupling of ionic states with the continuum of metal conduction-band states and is represented in a basis of asymptotic projectile states. Diagonalization of the self-energy matrix yields complex eigenvalues

$\omega_j(D)$ and the eigenvectors ('resonance states') $|\phi_j(D)\rangle$ where j collectively denotes all quantum numbers. Resonance energies and widths are given by $E_j(D) = \mathrm{Re}\,\omega_j(D)$ and $\Gamma_j(D) = -2\,\mathrm{Im}\,\omega_j(D)$, respectively. Many-body effects, in particular the Pauli-exclusion principle, are not incorporated. As a consequence, the resonance width can be related to either the resonant capture rate or the rate of resonant loss into empty conduction band states.

Inserting (3.2) into (3.1) leads to the close-coupling equations

$$\dot{c}_j(t) = -\sum_{j'=1}^{N} c_{j'}(t)\left\langle \phi_j(D(t))\middle|\frac{\mathrm{d}}{\mathrm{d}t}\right. + \frac{\Gamma_j}{2}\delta_{jj'}\left|\phi_{j'}(D(t))\right\rangle \times \exp\left[-\mathrm{i}\int^{t}\mathrm{d}t'\,(E_{j'} - E_j)\right]. \tag{3.3}$$

Dynamical couplings between the resonance states $|\phi_j(D)\rangle$ are mediated by the operator $\mathrm{d}/\mathrm{d}t = -v\mathrm{d}/\mathrm{d}D$ (v is the component of the ion velocity perpendicular to the surface.). For a given initial population $\{c_j(t = -\infty)\}$, the probability $P_1(t)$ for ionization to occur until time t is

$$P_1(t) = 1 - \sum_{j=1}^{N} |c_j(t)|^2. \tag{3.4}$$

3.2. Resonance energies and widths

In Fig. 5 the resonance energies emerging from the $(n = 2;\ m = 0)$ manifold are shown in comparison with results of other non-perturbative methods. Nordlander and Tully used a complex scaling method [11,12], Borisov et al. their coupled angular mode method [9], Martin and Politis a multicenter Gaussian expansion [14], and Deutscher et al. a stabilized single center expansion [15]. There is good agreement of our results with the other calculations and minor differences in the electronic potentials used by the various authors appear to have only a small influence.

Fig. 6 shows the $(m = 3)$-resonance energies of the $(n = 5)$- to $(n = 7)$-manifolds and Fig. 7 the widths of the $(n = 7,\ m = 3)$-manifold for Be^{3+}

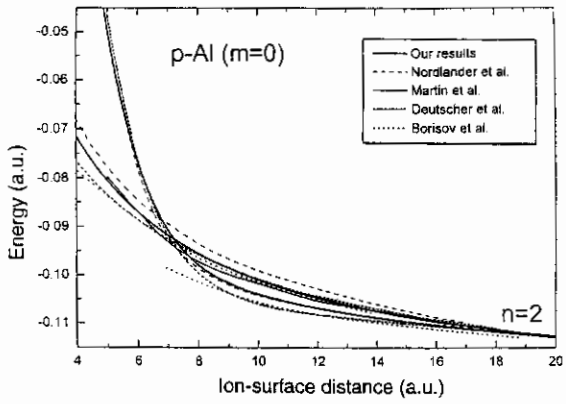

Fig. 5. Comparison of the resonance energies for $(m = 0)$-states emerging from the asymptotic $(n = 2)$-manifold and the results of Nordlander and Tully [11,12], Borisov et al. [9], Martín and Politis [14], and Deutscher et al. [15].

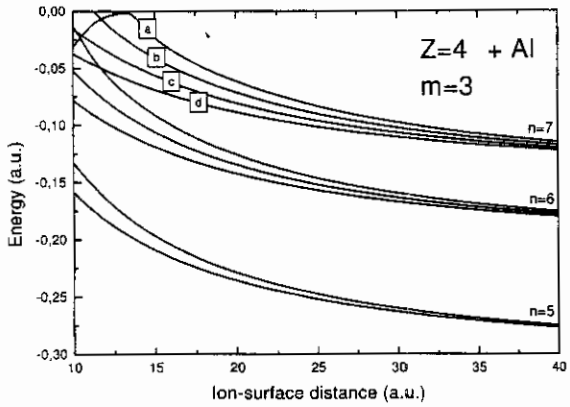

Fig. 6. Energies of the $(m = 3)$-resonances states of the asymptotic $(n = 5)$- to $(n = 7)$-manifolds for a nuclear charge $Z = 4$ near an Al-surface. The labels 'a' and 'd' refer to the widths in Fig. 7 and to the density plots in Figs. 8a and d.

and an Al-surface. The behavior in the shifts is similar to the shifts of the $(m = 0)$-states (Fig. 5) and is mainly driven by the repulsive nuclear image potential.

3.3. Orbital hybridization

Contour plots of the electronic probability density in a plane perpendicular to the surface and

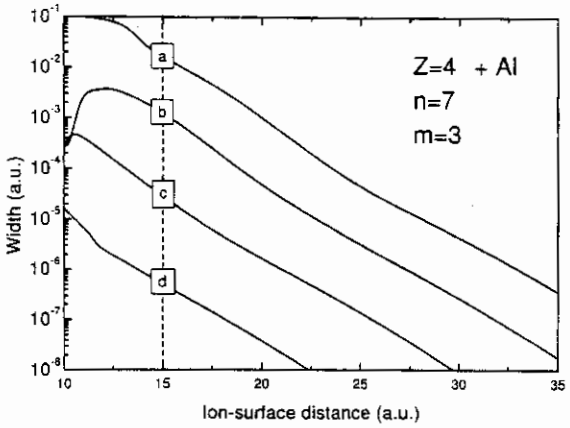

Fig. 7. Widths of the $(n = 7;\ m = 3)$-resonances states for a nuclear charge $Z = 4$ near an Al surface. The labels 'a' and 'd' and the vertical dashed line refer to the energies in Fig. 6 and density plots shown in Figs. 8a and d.

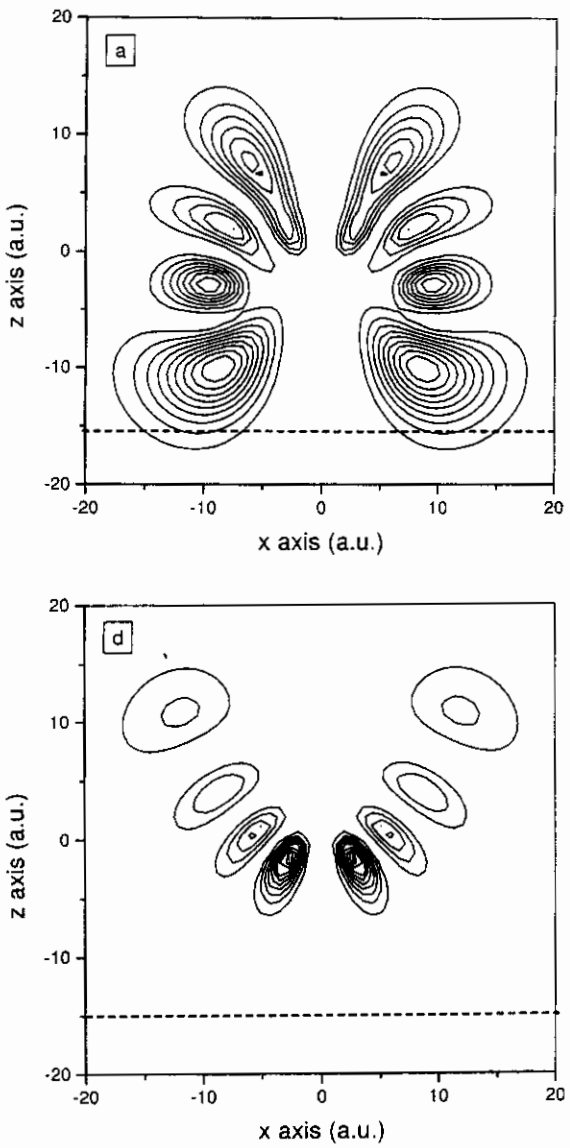

Fig. 8. Charge density of surface resonances in the plane perpendicular to the surface and containing the ionic nucleus of charge $Z = 4$. The ion–surface distance is 15 a.u. We used a reference frame with the origin at the ion. The dashed line marks the surface edge. The labels 'a' and 'd' refer to the energies in Fig. 6 and widths in Fig. 7.

including the ionic nucleus of resonance wavefunctions for the asymptotic $(n = 7,\ m = 3)$-manifold at a distance $D = 15$ a.u. are presented in Fig. 8. The dashed line corresponds to the surface location. While state 'a' tends to point towards the surface, state 'b' exhibits a charge density oriented towards the vacuum resulting in a decrease of the width by almost five orders of magnitude.

The shape of resonance wavefunctions changes as a function of D (not shown [19]). While approaching the surface, the electron density of resonance 'a' tends to bend towards the surface which leads to a slight increase in the exponential slope of the corresponding width in the ion–surface distance range of 12.5–15 a.u. (cf. Fig. 7) and is related to the onset of the downward level shift (cf. Fig. 6). The analysis of the resonance states in terms of parabolic states shows that strong deviations from a Stark-like behavior occur at ion–surface distances smaller than the classical radius [19].

3.4. Resonance ionization in electric fields

In an experimental setup devised for the study of resonance ionization of Rydberg atoms [40], an external electric field is used to remove ions from the surface. An additional static external electric field leads to the *Stark* splitting of the asymptotic (n, m)-manifolds. Fig. 9 shows nonperturbative energies and widths of resonance states for the asymptotic $(n = 4, 5, 6;\ m = 0)$-manifolds for a

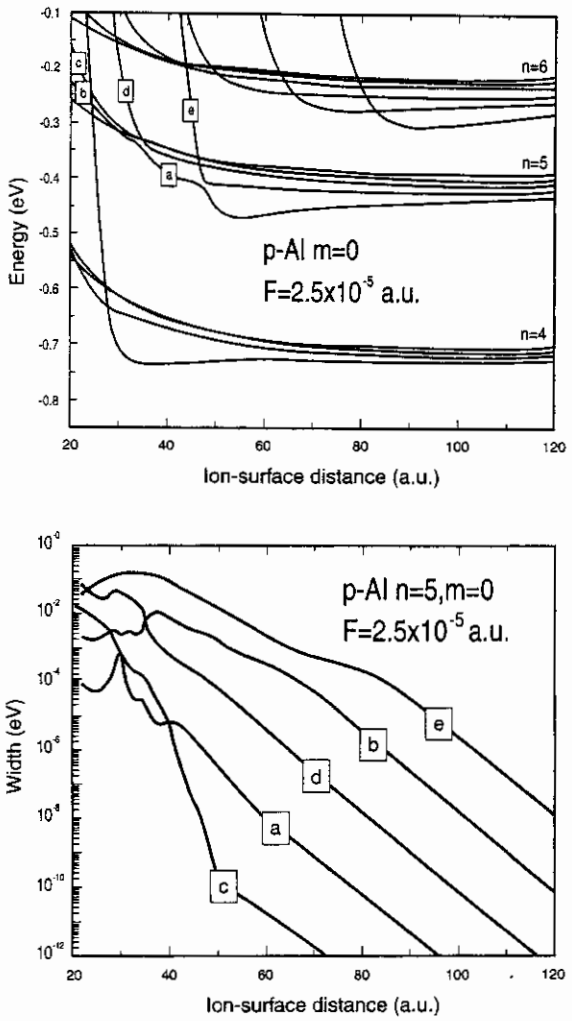

Fig. 9. (a) Energies of the resonance states asymptotically converging to the $(n = 4, 5, 6;\ m = 0)$-manifolds for an external electric field of strength $F = 2.5 \times 10^{-5}$ a.u.; (b) Widths for the asymptotic $(n = 5;\ m = 0)$-manifold. Labels 'a'–'e' refer to energies and widths of the same resonance state.

field strength of 2.5×10^{-5} a.u. $= 1.3 \times 10^{5}$ V/cm. Compared to field-free calculations, this external electric field tends to preserve the overall structure of the level diagram and is by far too weak to allow for field ionization.

In order to investigate the velocity dependence of dynamic couplings between the resonance states as the ion approaches the surface, we performed calculations for perpendicular velocities in the range of $v = 2 \times 10^{-5}$ to 2×10^{-2} a.u., both for the field-free case and for an external electric field of 2.5×10^{-5} a.u., directed to retract positive ions from the surface. We solved Eq. (3.3) for excited hydrogen atoms with an initial statistical population of the $(n = 5;\ m = 0)$-manifold [20].

In the region of sub-thermal velocities ($v = 2 \times 10^{-5}$ a.u.) relevant for proposed experiments [41,42], dynamic couplings play a very minor role [20]. The discrepancies between our results with and without dynamical couplings are further reduced if the external electric field is applied, since *Stark* splittings induced by the external field diminish the effect of off-diagonal couplings. We note that classical rate equations similar to those used by Nordlander and Dunning [41,42] can be reproduced from our quantum approach by suppressing off-diagonal dynamical couplings in the close coupling equation (3.1). When raising the perpendicular velocity of the ion to the thermal velocity of 10^{-3} a.u., the ionization probability P_I becomes sensitive to dynamical couplings. At $v = 2.048 \times 10^{-2}$ a.u. dynamic couplings lead to a 30% higher ionization probability as compared to the rate-equation-like uncoupled case (Fig. 10).

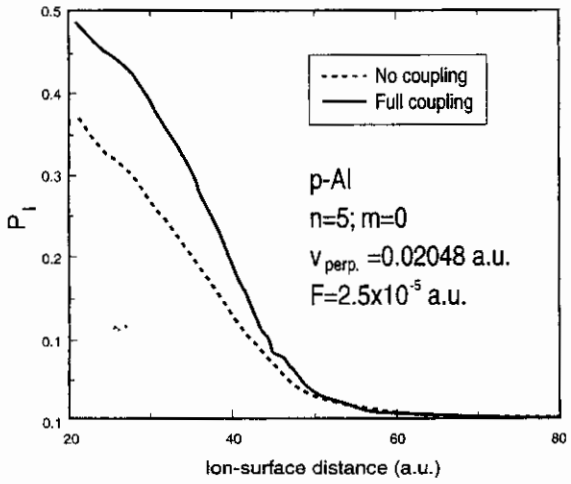

Fig. 10. Total ion production for $F = 2.5 \times 10^{-5}$ a.u. The normal velocity is 2.048×10^{-2} a.u. Dashed line: no dynamic coupling. Full line: full dynamic coupling.

4. Summary

We have included atomic structure calculations, Monte-Carlo sampling along the entire reflected projectile trajectory and the modeling of PO, SF, and CP within an extended COM. Our simulation results are in good agreement with measured projectile kinetic energy gains, electron emission yields, and final charge-state distributions for non-penetrating collisions of HCIs with surfaces.

Detailed quantum mechanical single-electron close-coupling calculations may provide improved input data for the refinement of COMs. The self-energy method allows for the efficient computation of level shifts and widths. We used this method for the generation of surface resonances (for nuclear charges up to $Z = 4$ near a metal surface) that serve as ('molecular') basis functions for the solution of the time-dependent Schrödinger equation. Our results for ion yields in collisions of H with an Al-surface show that quantum mechanical dynamic couplings play a minor role at sub-thermal velocities but lead to a significant rearrangement of the charge density for perpendicular velocities greater than 10^{-3} a.u.

Acknowledgements

This work was supported by the Division of Chemical Sciences, Office of Basic Energy Sciences, Office of Science, U.S. Department of Energy and by the National Science Foundation under grant PHY-9604872.

References

[1] A. Arnau et al., Surf. Sci. Rep. 27 (1997) 113.
[2] J. Burgdörfer, in: C.D. Lin (Ed.), Review of Fundamental Processes and Applications of Atoms and Ions, World Scientific, Singapore, 1993.
[3] J. Burgdörfer, P. Lerner, F.W. Meyer, Phys. Rev. A 44 (1991) 5674.
[4] J. Burgdörfer, C. Reinhold, F. Meyer, Nucl. Instr. and Meth. B 98 (1995) 415.
[5] J. Thomaschewski, J. Bleck-Neuhaus, M. Grether, A. Spieler, N. Stolterfoht, Phys. Rev. A 57 (1998) 3665.
[6] J. Ducrée, F. Casali, U. Thumm, Phys. Rev. A 57 (1998) 338.
[7] J. Ducrée, H.J. Andrä, U. Thumm, Phys. Scripta, to appear.
[8] U. Thumm, J. Phys. B 25 (1992) 421.
[9] A.G. Borisov, D. Teillet-Billy, J.P. Gauyacq, Nucl. Instr. and Meth. B 78 (1993) 49.
[10] A.G. Borisov, R. Zimny, D. Teillet-Billy, J.P. Gauyacq, Phys. Rev. A 53 (1996) 2457.
[11] P. Nordlander, J.C. Tully, Phys. Rev. Lett. 61 (1988) 990.
[12] P. Nordlander, J.C. Tully, Phys. Rev. B 42 (1990) 5564.
[13] P. Nordlander, Phys. Rev. B 53 (1996) 4125.
[14] F. Martín, M.F. Politis, Surf. Sci. 356 (1996) 247.
[15] S. Deutscher, X. Yang, J. Burgdörfer, Phys. Rev. A 55 (1997) 466 and private communication.
[16] P. Kürpick, U. Thumm, Phys. Rev. A 54 (1996) 1487.
[17] P. Kürpick, U. Thumm, U. Wille, Phys. Rev. A 56 (1997) 543 and references therein.
[18] P. Kürpick, U. Thumm, U. Wille, Nucl. Instr. and Meth. B 125 (1997) 273.
[19] P. Kürpick, U. Thumm, Phys. Rev. A 58 (1998) 2174.
[20] P. Kürpick, U. Thumm, U. Wille, Phys. Rev. A 57 (1998) 1920.
[21] L. Hägg, C.O. Reinhold, J. Burgdörfer, Phys. Rev. A 55 (1997) 2097.
[22] A.G. Borisov, V. Sidis, H. Winter, Phys. Rev. Lett. 77 (1996) 1893.
[23] F. Aumayr, Proc. XIX. ICPEAC, Whistler, Canada, 1995, AIP Conf. Proc., vol. 306, AIP Press, Woodbury, NY, 1995.
[24] J. Ducrée et al., Phys. Rev. A 57 (1998) 1925.
[25] J. Ducrée, J. Mrogenda, E. Reckels, H.J. Andrä, Nucl. Instr. and Meth. B 145 (1998) 509.
[26] F.W. Meyer, L. Folkerts, H.O. Folkerts, S. Schippers, Nucl. Instr. and Meth. B 98 (1995) 441.
[27] L. Folkerts, S. Schippers, D.M. Zehner, F.W. Meyer, Phys. Rev. Lett. 74 (1995) 2204.
[28] L. Folkerts, S. Schippers, D.M. Zehner, F.W. Meyer, Erratum, Phys. Rev. Lett. 75 (1995) 983.
[29] D. Niemann et al., Phys. Rev. A 56 (1997) 4774.
[30] S. Winecki, C.L. Cocke, D. Fry, M.P. Stöckli, Phys. Rev. A 53 (1996) 4228.
[31] R. Díez Muiño, N. Stolterfoht, A. Arnau, A. Salin, P.M. Echenique, Phys. Rev. Lett. 76 (1996) 4636.
[32] R. Díez Muiño, A. Salin, N. Stolterfoht, A. Arnau, P.M. Echenique, Phys. Rev. A 57 (1998) 1126.
[33] R.D. Cowan, The Theory of Atomic Structure and Spectra, University of California Press, Berkeley, CA, 1981.
[34] C. Lemell, H.P. Winter, F. Aumayr, J. Burgdörfer, F. Meyer, Phys. Rev. A 53 (1996) 880.
[35] C. Auth, T. Hecht, T. Igel, H. Winter, Phys. Rev. Lett. 74 (1995) 5244.
[36] C. Auth, H. Winter, Phys. Lett. A 217 (1996) 119.
[37] R. Baragiola, private communication.
[38] J. Hansen, O. Schraa, N. Vacek, Phys. Scripta T41 (1992) 41.
[39] S. Schippers, J. Limburg, J. Das, R. Hoekstra, R. Morgenstern, Phys. Rev. A 50 (1994) 540.

[40] D.F. Gray, Z. Zheng, K.A. Smith, F.B. Dunning, Phys. Rev. A 38 (1988) 1601.
[41] P. Nordlander, F.B. Dunning, Phys. Rev. B 53 (1996) 8083.
[42] P. Nordlander, F.B. Dunning, Nucl. Instr. and Meth. B 125 (1997) 300.
[43] J. Burgdörfer, E. Kupfer, H. Gabriel, Phys. Rev. A 35 (1987) 4963.